

Electromagnetic, atomic-structure and chemistry changes induced by Ca-doping of low-angle $\text{YBa}_2\text{Cu}_3\text{O}_{7-\delta}$ grain boundaries

XUEYAN SONG, GEORGE DANIELS, D. MATT FELDMANN, ALEX GUREVICH,
DAVID LARBALESTIER*

Applied Superconductivity Center, University of Wisconsin, Madison, WI 53706, USA

Practical high temperature superconductors must be textured to minimize the reduction of the critical current density J_{gb} at misoriented grain boundaries. Partial substitution of Ca for Y in $\text{YBa}_2\text{Cu}_3\text{O}_{7-\delta}$ has shown significant improvement in J_{gb} but the mechanisms are still not well understood. Here we report atomic-scale, structural and analytical electron microscopy combined with transport measurements on 7° [001]-tilt $\text{Y}_{0.7}\text{Ca}_{0.3}\text{Ba}_2\text{Cu}_3\text{O}_{7-\delta}$ and $\text{YBa}_2\text{Cu}_3\text{O}_{7-\delta}$ grain boundaries, where the dislocation cores are well separated. We show that the enhanced carrier density, higher J_{gb} and weaker superconductivity depression at the Ca-doped boundary result from a strong, non-monotonic Ca segregation and structural rearrangements on a scale of ~ 1 nm near the dislocation cores. We propose a model of the formation of Ca^{2+} solute atmospheres in the strain and electric fields of the grain boundary and show that Ca doping expands the dislocation cores yet enhances J_{gb} by improving the screening and local hole concentration.

Second generation superconducting coated conductors (CCs) made from $\text{YBa}_2\text{Cu}_3\text{O}_{7-\delta}$ (YBCO), have great application potential¹ but conductor design remains severely constrained by the need for biaxial texture to avoid the exponential decrease of the critical current density $J_{\text{gb}}(\theta)$ through grain boundaries (GBs) with increasing misorientation angle θ above $3\text{-}5^\circ$ ^{2,3,4}. The most viable routes to CCs require deposition of $(\text{RE})\text{Ba}_2\text{Cu}_3\text{O}_{7-\delta}$ onto metal tapes textured by ion-beam assisted deposition^{5,6} or oxide-buffered, rolling-assisted bi-axially textured Ni-alloy substrates⁷. However, even the best CCs have many GBs with $\theta \approx 5\text{-}7^\circ$ which partially obstruct current. The current-blocking effect of GBs⁸⁻¹³ in YBCO can indeed be mitigated by Ca doping, but the mechanisms by which Ca improves J_{gb} are still not well understood. The positive effect of Ca-doping is believed to result from a partial replacement of Y^{3+} by Ca^{2+} , which increases the hole carrier density at the GB¹³. Thus, despite reduction of T_c in Ca doped YBCO¹³, J_{gb} at $T \ll T_c$ can be ameliorated both by Ca addition^{8,10} and by annealing in oxygen⁹. It has been recently realized that J_{gb} is mostly controlled by weakened superconductivity due to strain and charging effects^{10,14} in the nanoscale channels between the GB dislocations. Significant GB charging was indeed revealed by electron holography of 4° [001]-tilt pure and Ca-doped YBCO bicrystals¹⁵ for which the negative GB potential was smaller (-1 V vs. -2.4 V) and decayed over a shorter length (0.8 nm vs. 1.7 nm) for the Ca-doped GB. However, detailed nanoscale structural characterization of doped and undoped grain boundaries that explains the effect of Ca substitution is still lacking.

In this paper we investigate the lattice structure, electronic state and current transport of pure and Ca-doped GBs in low-angle YBCO bicrystals by combining measurements of extended voltage-current (V-I) characteristics on a matched pair of Ca-doped and pure 7° [001]-tilt YBCO bicrystals, and detailed atomic-scale microscopy and local composition of the same GBs. We found a significant Ca segregation to the GB and a non-monotonic variation of Ca concentration around the dislocation cores on scales ~ 1 nm. The structural changes induced by Ca doping expand the dislocation cores both normal and parallel to the GB, yet surprisingly *increase* J_{gb} close to the critical current density J_g in the grains. The totality of our high resolution electron microscopy and transport data indicates that this local Ca segregation significantly

reduces the superconductivity depression at the GB and improves vortex pinning in magnetic fields.

V-I characteristics, J_g and J_{gb} measured after post-annealing in oxygen for 30 minutes at 420°C are shown in Figure 1. This treatment put both samples into the overdoped state with $T_c = 91$ K for YBCO and 71 K for the 0.3Ca-doped samples. The data are compared at the same reduced temperature $T/T_c = 0.86$ (78 K for the pure and 61 K for the Ca-doped YBCO). The J_{gb}/J_g ratio measured at the electric field $E = 1$ $\mu\text{V}/\text{cm}$ varies from $J_{gb}/J_g < 1$ at low magnetic fields B to $J_{gb}/J_g \approx 1$ at $B \approx 3\text{--}4$ T for both samples. J_{gb}/J_g is much smaller for the pure YBCO than for the Ca-doped film, and J_{gb} for the Ca-doped film is higher, even though it has a lower J_g than YBCO. At lower B , YBCO exhibits a kink in the $\log E$ - $\log J$ plot at $J \approx J_{gb}$, unlike the smooth $\log E$ - $\log J$ intragrain traces. By contrast, the Ca-doped GB exhibits much more gradual $\log E$ - $\log J$ characteristics. These differences are evident in the linear E - J plots, which show a pronounced ohmic resistance R_F for pure YBCO, but rather nonlinear $E(J)$ for the Ca-doped YBCO at $J > J_{gb}$. In either case J_{gb} falls below J_g because of depressed superconductivity at the GB.

We performed extensive transmission electron microscopy (TEM) of the GBs from the micron to the atomic-scale. Both the pure and Ca-doped GBs were rather straight with $\sim 85\%$ (100) GB segments, connected by short facets along (110) and (100), as shown in Figure 2. The [100] dislocations separate channels through which current flows. The GB shows up very well under high-angle annular dark-field (HAADF) Z-contrast imaging whose intensity $W \propto Z^{1.7}$ depends on the atomic number $Z^{17,18}$, differentiating the brighter Y/Ba from darker Cu/O(4) columns. The Z-contrast images and atomic stacking patterns of Figure 3a show that [100] dislocation cores in pure YBCO GB have 2 Cu/O columns surrounded by 5 Y/Ba columns. Contrast immediately below the terminating Y/Ba column is poor but intensity traces taken a little lower indicate that the Cu/O columns are continuous across the expanded, tensile region of the dislocation.

Figure 3b shows a Z-contrast image of the Ca-doped film in which the brighter columns contain Y/Ba/Ca atoms. The [100] dislocation is again defined by one missing Y/Ba/Ca column, but the contrast immediately below this terminating column

in the tensile region is noticeably different. Two bright columns with similar intensity to the neighboring intragrain Y/Ba/Ca columns appear at the expected Cu/O column sites. The arrow in Figure 3b marks a third anomalous column which is *darker* than the neighboring Cu/O columns. These two bright and one dark column are consistently observed in every tensile segment of the Ca-doped GB. These images show that the dislocation core region is also significantly expanded perpendicular to the GB plane, as shown in Figure 3c, while the tensile part of the dislocation extends along the Ca-doped GB over 3 unit cells, rather than the 1-2 cells in pure YBCO.

Electron energy loss spectra (EELS) were measured both perpendicular and parallel to the GB with a 0.2 nm electron probe and a stage-drift-limited spatial resolution of 0.3-0.4 nm. Figure 4a compares Ca L_{23} edge spectra averaged from 10 different individual dislocation cores and 15 intragrain regions. The data show that the Ca content of 0.46 in the tensile part of the dislocation core exceeds the nominal bulk Ca concentration by 55%. Spectral traces normal to the GB revealed sharp Ca peaks at the GB, and pronounced minima about 2 unit cells away, as shown in Figure 4b. Moreover, the Ca concentration varies *non-monotonically* along the GB near the 2 bright-1 dark column triplet at the dislocation core in Figure 4c. The single dark column in the Z-contrast images is another indication of strong local Ca-enrichment.

Oxygen K-edge EELS spectra at the dislocation cores in Figure 5 clearly show a pre-peak around 528 eV indicative of metallic behavior, both for the pure and Ca-doped GB. Although EELS imaging damaged the cores within a few seconds, we were able to measure a lower hole deficiency at the Ca-doped GB. For a nearly optimally doped $\text{YBa}_2\text{Cu}_3\text{O}_{7-\delta}$ with $\delta \approx 0.2$, the oxygen K-edge at 535 eV is coupled to the pre-peak at 528 eV by transitions to the O-2p states, which form the hole valence band. As δ increases, the intensity of the 528 eV peak falls, indicating a decrease in the hole concentration and a reduction of T_c ¹⁹. Electron beam damage makes spatial variations of the oxygen K-edge pre-peak intensity inconclusive, yet the EELS results also indicate that neither the pure nor the Ca-doped GB dislocation cores are strongly hole-deficient. This result is consistent with earlier lower spatial resolution (~ 2 -3 nm) data taken on low-angle, flux-grown, bulk [001]-tilt bicrystals, which exhibited only weak depression of the oxygen pre-peak near the GB²⁰.

The structure of the pure dislocation core in Figure 3a is also consistent with earlier studies of [100] dislocations at YBCO GBs²¹. However, we found for the first time that Ca not only expands the dislocation cores, but that the structure of the Ca-doped core is different from the pure one, as shown by the unusual column intensity sequence in Figure 3b. For instance, the Ca-induced core expansion may result from a stacking fault $(Y/Ba/Ca)/(Cu/O)/(Y/Ba/Ca)/(Y/Ba/Ca)/(Y/Ba/Ca)/(Cu/O)/(Y/Ba/Ca)$ in the dislocation tensile region. The stacking fault could result from the dislocation reaction, $[100] \rightarrow \frac{1}{2} [100] + \frac{1}{2} [100]$. In any case, the striking aspect of the Ca segregation shown in Figure 4 is its strong variation along the GB on the scale of the unit cell, indicating that the larger Ca^{2+} ion of radius $r_{ca} = 0.099$ nm may preferentially substitute for the smaller Y^{3+} ($r_Y = 0.09$ nm) in the tensile part of the dislocation core²². The segregation of solute can strongly affect the structure of GBs²³⁻²⁵, for example, Ca segregation can induce the GB lattice transformation in MgO ²⁵.

The surprising result of our microscopy is that the undisturbed channel between the dislocation cores was narrowed, yet our transport data show a higher J_{gb} for the Ca-doped bicrystals over a wide range of field and temperature, in agreement with prior studies^{9,11,15}. Here J_{gb} is limited by pinning of the GB vortices whose structure changes dramatically as compared to the bulk Abrikosov vortices. Indeed, depressed superconductivity at the GB due to charging, d-wave symmetry and local non-stoichiometry causes expansion of the GB vortex core from a normal core of the order of the intragrain coherence length $\xi \approx 4$ nm to a stretched Josephson core of length $\ell(T) \gg \xi$ along the GB¹⁶. The core size $\ell(T)$ along the GB is determined by the averaged GB depairing current density J_0 which can be extracted from the flux flow resistance, $R_F = [H/(H + H_0)]^{1/2} R$ at $J > J_{gb}$, where R is the normal-state GB resistance, $H_0 = \phi_0/(2\pi\ell)^2$ is the crossover field at which the GB vortex cores overlap, $\ell \approx \xi J_d/J_0$, J_d is the intragrain depairing current density, and ϕ_0 is the flux quantum¹⁶. Previous analysis of $R_F(H)$ of the pure 7° YBCO bicrystal with the GB dislocation spacing of 3.2 nm showed that $J_0 \approx 0.1J_d$ and $\ell \approx 10\xi$ at 77 K, while the temperature dependence of $J_0 \propto (1 - T/T_c)^2$ indicates that current channels behave like strongly proximity-coupled, superconducting-normal-superconducting point contacts. However, Figure 1 shows that

Ca-doping reduces the difference between the intragrain and intergrain E-J characteristics, shrinking the GB vortex core size ℓ and increasing J_0 . In fact, the difference between J_0 and J_d for the Ca-doped bicrystal becomes so small that the analysis of Ref. 16 cannot distinguish GB vortices from bulk vortices, indicating only weak superconductivity depression on the GB. This increase of J_0 results from reduction of the average sheet GB charge density Q , the local electric potential $\varphi_0 = 2\pi l_D Q/\varepsilon$, and the Thomas-Fermi screening length l_D produced by partial substitution of Y^{3+} by Ca^{2+} where ε is the lattice dielectric constant. Because the negative potential φ_0 drives the superconducting state at the hole-deficient GB toward the antiferromagnetic insulator characteristic of the high- T_c cuprates¹⁴, Ca-doping improves J_{gb} both by reducing Q and l_D , as recently shown by electron holography of Ca-doped YBCO bicrystals¹⁵. The strain-induced GB charge¹⁴ $Q \propto b^2$ can also be reduced by as much as half by splitting the GB dislocation into partial dislocations with Burgers vectors $b/2$.

To understand the non-monotonic Ca distribution, we consider the equilibrium concentration $c(\mathbf{r})$ of Ca in the pressure field $p(x,y)$ and the screened electric potential $\varphi(\mathbf{r})$ produced by the GB dislocations^{14,26,27,28}.

$$c = \frac{c_0}{c_0 + (1 - c_0) \exp[(p\Delta V + \varphi\Delta Z)/k_B T]} \quad (1)$$

Here $\Delta V = V_{Ca} - V_s$ and $\Delta Z = Z_{Ca} - Z_s$ are the differences of ionic volumes and charges of the Ca and the substituted atom (Y), c_0 is the bulk concentration, $p(x,y) = p_0 \sin(2\pi y/d)/[\cosh(2\pi\rho/d) - \cos(2\pi y/d)]$, $d = b/2\sin(\theta/2)$ ²⁸, $p_0 = \mu\sin(\theta/2)/(1-\nu)$, $\rho = (r_0^2 + x^2)^{1/2}$, the cutoff radius $r_0 \sim b$ accounts for the plastically deformed dislocation core, μ is the shear modulus, ν is the Poisson coefficient, and x and y are coordinates across and along the GB, respectively. The distribution of Ca concentration, $c(x,y)$ plotted in Figure 6 exhibits peaks in tensile regions followed by pronounced dips in compressed regions along the GB, and a non-monotonic dependence of $c(x)$ across the GB, in good agreement with our EELS data in Figure 4. Equation (1) also shows that the periodic stress $p(y)$ tends to increase the average Ca concentration at the GB, $\langle c \rangle = \int^L c(x,y)dy/L$ where $L \gg d$. For $p_0\Delta V/k_B T \ll 1$, $\varphi = 0$, and $c_0 \ll 1$, we obtain $\langle c(x,y) \rangle = c_0 \langle \exp[-\Delta V p(x,y)/k_B T] \rangle \approx c_0(1 + \Delta V^2 \langle p^2 \rangle / 2k_B^2 T^2) > c_0$, where $\langle p \rangle = 0$, and $\langle p^2 \rangle = 2p_0^2/[\exp(4\pi\rho/d)]$.

– 1]. Taking $\nu = 0.3$, $\mu = 40\text{GPa}$, $\theta = 7^\circ$, $\Delta V = V_{\text{Ca}} - V_{\text{Y}} = 4\pi(r_{\text{Ca}}^3 - r_{\text{Y}}^3)/3$, ionic radii $r_{\text{Ca}} = 0.099\text{ nm}$, $r_{\text{Y}} = 0.09\text{ nm}$ and $T = 300\text{ K}$, we estimate $p_0\Delta V/k_{\text{B}}T_i \approx 0.85$. Thus, the GB dislocation strains favor segregation of Ca, partially offsetting the electrostatic barrier caused by the negative $\phi(x)$ of a hole-deficient GB. For $Z_{\text{Ca}} < Z_{\text{Y}}$, the competition between strain and electric field effects causes minima in $c(x)$, as shown in Figures 4 and 6. Similar minima in $\phi(x)$ were revealed by electron holography of a 4° Ca-doped YBCO bicrystal¹⁵.

This model can explain our observation that Ca doping actually increases $J_{\text{gb}}(H)$ despite shrinkage of the current channels and expansion of the dislocation cores. As follows from Figure 6, this structural expansion naturally results from increased lattice disorder produced by the Cottrell atmosphere²⁸ of segregated Ca^{2+} ions. However, because Ca^{2+} brings extra holes to the GB, superconductivity in the cores is enhanced by partial recovery of optimum hole doping. This enhancement occurs highly non-uniformly: Ca segregates mostly in the tensile regions of the GB, while compressed regions have markedly less Ca than the bulk. The Ca-enriched charged dislocation cores are coupled across the channels by the electric potential $\phi(x,y)$ due to hole redistribution, which reduces ϕ_0 , Q and I_D . As a result, the overall J_{gb} increases, because the compressed Ca-deficient current channels exhibit much less T_c depression than bulk Ca-doped YBCO, yet they have less hole depletion than in pure YBCO due to the lower charge and shorter I_D near the dislocation cores.

Our model suggests new possibilities for manipulating the properties of doped GBs. An equilibrium Ca distribution initially forms at the film growth or annealing temperature, but then evolves according to Eqn. (1) as $T(t)$ decreases. The equilibration time $t_d \sim l_0^2/D$ of the Cottrell atmosphere is controlled by the Ca diffusivity $D = D_0\exp(-U/k_{\text{B}}T)$ with $U \sim 1\text{-}2\text{ eV}$ ²⁹ over a small strained region of radius $l_0 \sim d/2\pi \sim 1\text{ nm}$ around the dislocation cores. Taking $D(300\text{ K}) \sim 10^{-16}\text{ cm}^2/\text{s}$ in the ab-plane²⁹ we obtain $t_d \sim 10^2\text{ s}$ at room temperature, but because $t_d(T)$ increases very rapidly as T decreases below 300 K, the segregation of Ca effectively freezes at a temperature T_i well above T_c . Thus, aging effects may occur below 300 K, consistent with sometimes variable behavior observed on Ca-doped GBs. This model suggests that Ca

segregation can also be controlled by the oxygen annealing conditions⁹, which can cause charge-driven GB overdoping, reduce the electrostatic barrier φ_0 , and facilitate further segregation of Ca at the GB. Such strain and charge-driven diffusion segregation of Ca to the GB²⁹ probably underlies the positive overdoping effects observed in YBCO/(Y,Ca)BCO multilayers⁸. In a recent preprint R. Klie et al. reported atomic-resolution TEM, EELS, and density functional calculations, which indicate that strains produced by the mismatch of Ca-O and Cu-O atomic bond lengths are very important for Ca segregation on YBCO grain boundaries³¹.

In conclusion, our atomic-scale electron microscopy and transport measurements show that the enhanced critical current densities of Ca-doped YBCO bicrystals result from inhomogeneous Ca segregation to the grain boundary, structural expansion of the dislocation cores and non-monotonic Ca distribution both along and across the boundary on a scale ~ 1 nm. This Ca segregation causes shrinkage of the GB vortex cores and improved flux pinning, increased hole concentration and reduction of the GB charge and screening length. The beneficial effect of Ca doping at $T < T_c$ is explained by formation of quenched distributions of Ca^{2+} dopants in the strain and electric fields of the dislocation cores. Our results suggest significant new opportunities for nanoscale impurity segregation engineering.

METHODS

Our c-axis oriented $\text{YBa}_2\text{Cu}_3\text{O}_{7-\delta}$ and $\text{Y}_{0.7}\text{Ca}_{0.3}\text{Ba}_2\text{Cu}_3\text{O}_{7-\delta}$ films of thickness 230 nm were grown by pulsed laser deposition on symmetric 7° [001]-tilt SrTiO_3 bicrystals⁹. After lithographic patterning transport properties of the films were measured from 10 to 90K in fields up to 12 T parallel to the c-axis⁹. Samples for plan-view TEM were prepared by mechanical polishing and ion milling. Diffraction contrast and high resolution TEM investigations were performed using a microscope (Philips CM200) operated at 200 KV with point resolution of 0.19 nm. HAADF imaging¹⁷ in a scanning TEM was performed using a 200 KV (JEOL 2010F) microscope focused to a ~ 0.14 nm diameter probe³⁰ with the inner cut-off angle of the HAADF detector > 52 mrad.

Transmitted electrons were analyzed by an on-axis electron-energy-loss spectrometer with an energy dispersion of 0.3 eV per channel and an energy resolution of ~1.2 eV.

-
1. Larbalestier, D., Gurevich, A., Feldmann, D. M. & Polyanskii, A. High-T_c superconducting materials for electric power applications. *Nature* **414**, 368-377 (2001).
 2. Verebelyi, D. T. *et al.* Low angle grain boundary transport in YBa₂Cu₃O_{7-δ} coated conductors. *Appl. Phys. Lett.* **76**, 1755–1757 (2000).
 3. Feldmann, D. M. *et al.* Influence of nickel substrate grain structure on YBa₂Cu₃O_{7-δ} supercurrent connectivity in deformation-textured coated conductors. *Appl. Phys. Lett.* **77**, 2906-2908 (2000).
 4. Hilgenkamp, H. & Mannhart, J. Grain boundaries in high-T_c superconductors. *Rev. Mod. Phys.* **74**, 485-549 (2002).
 5. Arendt, P.N. & Foltyn, S. R. Biaxially textured IBAD-MgO templates for YBCO-coated conductors. *MRS Bull.* **29**, 543-550 (2004).
 6. Iijima, Y., Kakimoto, K., Yamada, Y., Izumi, T., Saitoh, T. & Shiohara, Y. Research and development of biaxially textured IBAD-GZO templates for coated superconductors. *MRS Bull.* **29**, 564-571 (2004).
 7. Goyal, A., Paranthaman, M. P. & Schoop, U. The RABiTS Approach: Using rolling-assisted biaxially textured substrates for high-performance YBCO superconductors. *MRS Bull.* **29**, 552-560 (2004).
 8. Hammerl, G. *et al.* Enhanced supercurrent density in polycrystalline YBa₂Cu₃O_{7-δ} at 77 K from calcium doping of grain boundaries. *Nature* **407**, 162-164 (2000).
 9. Daniels, G. A., Gurevich, A. & Larbalestier, D. C. Improved strong magnetic field performance of low angle grain boundaries of calcium and oxygen overdoped YBa₂Cu₃O_{7-δ}. *Appl. Phys. Lett.* **77**, 3251-3253 (2000).
 10. Schmehl, A. *et al.* Doping induced enhancement of the critical currents of grain boundaries in YBa₂Cu₃O_{7-δ}. *Europhys. Lett.* **47**, 110–115 (1999).
 11. Guth, K., Krebs, H. U., Freyhardt, H. C. & Jooss, Ch. Modification of transport properties in low-angle grain boundaries via calcium doping of YBa₂Cu₃O_x thin films. *Phys. Rev. B* **64**, R140508-140512 (2001).
 12. Weber, A., Hammerl, G., Schmehl, A., Schneider, C. W. & Mannhart, J. Ca-doping-induced enhancement of the critical currents of coated conductors grown by ion-beam-assisted deposition. *Appl. Phys. Lett.* **82**, 772-774 (2003).
 13. Kucera J. T. & Bravman, J. C. Transport characterization of calcium-doped YBa₂Cu₃O_{7-δ} thin films. *Phys. Rev. B* **51**, 8582–8590 (1995).
 14. Gurevich, A. & Pashitski, E. A. Current transport through low-angle grain boundaries in high-temperature superconductors. *Phys. Rev. B* **57**, 13878-13893 (1998).
 15. Schofield, M. A., Beleggia, M., Zhu, Y., Guth, K. & Jooss, C. Direct evidence for negative grain boundary potential in Ca-doped and undoped YBa₂Cu₃O_{7-δ}. *Phys. Rev. Lett.* **92**, 195502/1-4 (2004).

-
16. Gurevich, A. *et al.* Flux flow of Abrikosov-Josephson vortices along grain boundaries in high-temperature superconductors. *Phys. Rev. Lett.* **88**, 097001/1-4 (2002).
 17. Voyles, P. M., Muller, D. A., Grazul, J. L., Citrin P. H. & Gossmann, H.-J. L. Atomic-scale imaging of individual dopant atoms and clusters in highly n-type bulk Si. *Nature* **416**, 826-829 (2002).
 18. Kirkland, E. J., Loane R. F. & Silcox, J. Simulation of annular dark field STEM images using a modified multislice method. *Ultramicroscopy* **23**, 77-96 (1987).
 19. Egerton, R. F. *Electron energy-loss spectroscopy in the electron microscope—2nd ed.* (Plenum Press, New York, 1996).
 20. Babcock, S. E. *et al.* A TEM-EELS study of hole concentrations near strongly and weakly coupled grain boundaries in electromagnetically characterized YBa₂Cu₃O_x bicrystals. *Physica C* **227**, 183–196 (1994).
 21. Browning, N. D. *et al.* The atomic origins of reduced critical currents at [001] tilt grain boundaries in YBa₂Cu₃O_{7-δ} thin films. *Physica C* **294**, 183-193 (1998).
 22. Flewitt P. E. J. & Wild, R. K. *Grain Boundaries: Their microstructure and chemistry.* (John Wiley & Sons LTD, Chichester, 2001).
 23. Udler D. & Seidman, D. N. Congruent phase transition at a twist boundary induced by solute segregation. *Phys. Rev. Lett.* **77**, 3379–3382 (1996).
 24. Maiti, A., Chisholm M. F., Pennycook, S. J. & Pantelides, S. T. Dopant segregation at semiconductor grain boundaries through cooperative chemical rebonding. *Phys. Rev. Lett.* **77**, 1306–1309 (1996).
 25. Yan, Y., Chisholm, M. F., Duscher, G., Maiti, A., Pennycook, S. J. & Pantelides, S. T. Impurity-Induced structural transformation of a MgO grain boundary. *Phys. Rev. Lett.* **81**, 3675–3678 (1998).
 26. Gurevich, A. & Pashitskii, E. A. Enhancement of superconductivity at structural defects in high-temperature superconductors. *Phys. Rev. B.* **56**, 6213-6225 (1997).
 27. Su, H. & Welch, D. O. The effects of space charge, dopants, and strain fields on surfaces and grain boundaries in YBCO compounds. *Supercond. Sci. Technol.* **18**, 24-34 (2005).
 28. Hirth, J.B. & Lothe, A. *Theory of dislocations.* (Mc Graw-Hill, New York, 1968).
 29. Berenov, A., Farvacque, C., Qi, X., MacManus-Driscoll, J. L., MacPhail, D. & Foltyn, S. Ca doping of grain boundaries. *Physica C* **372**, 1059-1062 (2002).
 30. James, E. M. & Browning, N D. Practical aspects of atomic resolution imaging and analysis in STEM. *Ultramicroscopy* **78**, 125-129 (1999).
 31. Klie, R. *et al.* Enhanced current transport at grain boundaries in high-T_c superconductors. *Nature*, 2005

Acknowledgements:

We are grateful to James Buban and Nigel Browning, formerly of the University of Illinois at Chicago, for experimental help, discussions and for access to the JEOL2010F there. We thank Steve Pennycook from ORNL for discussions. The work was supported by AFOSR under grant F49620-03-01-0429.

Correspondence and requests for materials should be addressed to D. L. at: larbalestier@engr.wisc.edu.

Figure Captions:

Figure 1. Critical current density vs. magnetic field, and electric field-current density (E-J) characteristics of the pure and 0.3Ca-doped films at the same reduced temperature $T/T_c = 0.86$. J_g and J_{gb} are evaluated at $1 \mu\text{V}/\text{cm}$, using V-I curves measured on $25 \mu\text{m}$ wide bridges produced by photolithographically patterning the links. The E-J characteristics for the pure YBCO GB segment show a steep rise in all magnetic fields below the irreversibility field of about 5 T due to preferential Abrikosov-Josephson vortex flow at the GB. The E-J characteristics of the Ca-doped GB are very much more similar to the intragrain E-J characteristics than is the case for the pure YBCO. The ohmic behavior with the resistance R_F due to vortex flow at the pure YBCO GB at $J > J_{gb}$ is indicated in the inset.

Figure 2. GB facet structure from the micron to the nano-scale of both pure (a) and 0.3Ca-doped (b) 7° [001]-tilt bicrystals, as examined by conventional TEM. The periodically spaced dislocation cores are evident by the white-appearing structures under higher magnification in Figure 2b.

Figure 3. Atomic structures of dislocation cores for pure and 0.3Ca-doped [001]-tilt YBCO grain boundaries.

(a) Z-contrast images of [100] dislocation cores for pure 7° [001]-tilt YBCO bicrystal. The Y-Ba and Cu-O columns are indicated in a-2.

(b) Z-contrast images of [100] dislocation cores for 0.3Ca-doped 7° [001]-tilt bicrystal. The expanded, more disordered tensile region of the dislocation core is indicated in b-2.

(c) Sketch of atomic column positions at [100] dislocation cores for the pure and 0.3Ca-doped GBs. Dashed lines indicate the dislocation cores regions

for pure YBCO GB and the expanded core regions for the Ca-doped GB. The gray marks three columns with anomalously intensity in the Ca-doped GB.

Figure 4. Ca segregation at the GB of the 0.3Ca-doped sample and Ca concentration variations perpendicular to and along the GB plane.

- (a) Averaged Calcium $L_{2,3}$ edge spectra acquired from the 10 dislocation cores and 15 intragrain regions away from the GB
- (b) Experimental data points of the Ca concentration variation in the direction perpendicular to the grain boundary. The solid curve shows the ratio $c(x)/c_0$ of the local Ca concentration $c(x)$ to the bulk value c_0 calculated from Eqn. (1) for $y = -0.2d$, and the parameters defined in the caption to Figure 6.
- (c) Experimental data points (taken from the yellow contours in the top Z-contrast image) of the Ca concentration variation along the grain boundary. The solid curve in the lower panel shows the ratio $c(x)/c_0$ calculated from Eqn.1 for the same values of the parameters as those in Figures 4b and 6.

Figure 5. Oxygen EELS spectra measured on the pure and 0.3Ca-doped GBs, showing evidence for significant 528 eV oxygen pre-peak right at the GB dislocation cores.

Figure 6. Surface plot of the distribution of Ca^{2+} solute ions near a periodic chain of edge dislocations in a 7° GB calculated from Eqn. (1), where $\varphi(x) = \varphi_0 \sum_n K_0[(r_0^2 + x^2 + (y - nd)^2)^{1/2}/l_D]/K_0(r_0/l_D)$, is a solution of the Thomas-Fermi equation $\nabla^2 \varphi - \varphi/l_D^2 = -4\pi q \sum_n f(x, y-dn)/\epsilon$ that describes the screened potential of charged dislocation cores spaced by d along the y -axis. Here $\varphi_0 = 2q/\epsilon$ is the amplitude of the electric potential produced by the line charge q per unit length of the core, $f(r)$ is a function which describes the radial distribution of charge density in a region of radius $\sim r_0 \ll d$, $\int f(x,y) dx dy = 1$, and $K_0(x)$ is a modified Bessel function. The values of the parameters are the same as those used to fit the EELS data in Figure 4: $c_0 = 0.3$, $\Delta V p_0/k_B T_i = 5.6$ (taking more realistic atomic bond lengths instead of the free ionic radii can significantly increase this parameter as compared to the estimate given in the text), $r_0 = 0.5b$, $l_D = 0.55 \text{ nm}$, $\Delta Z \varphi_0/k_B T_i = 26$, and $T_i \sim 300 \text{ K}$, in which case $\varphi_0 \approx 0.6 \text{ eV}$ is comparable to $\varphi_0 \approx 1 \text{ eV}$ deduced from electron holography study of a 4° 0.2Ca-doped GB¹⁵. The red peaks show Ca-enrichment of tensile regions of the dislocation cores, while blue regions show Ca-depleted current channels with much weaker T_c depression than in the bulk where $c_0 = 0.3$.

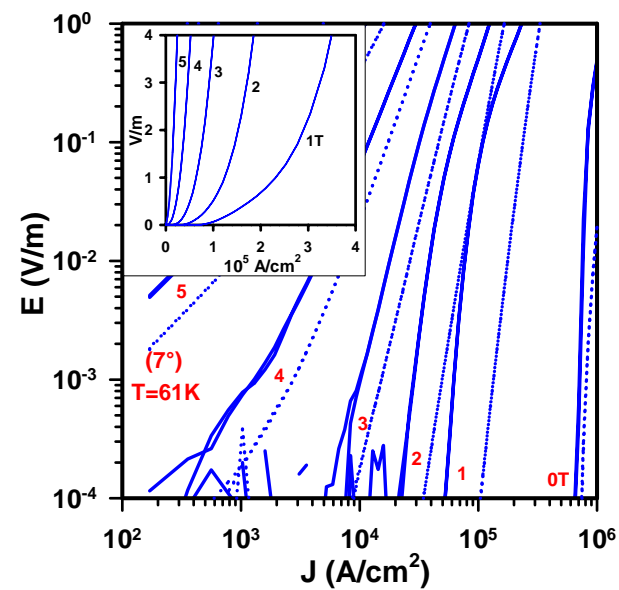
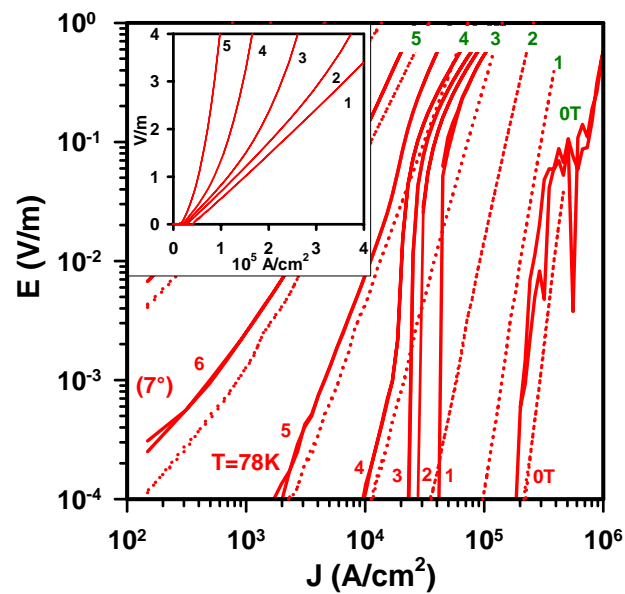
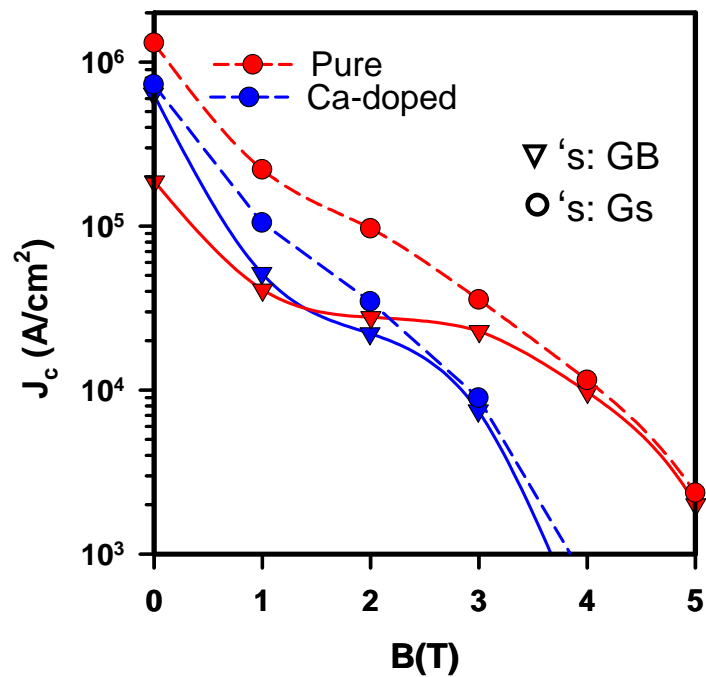


Figure 1

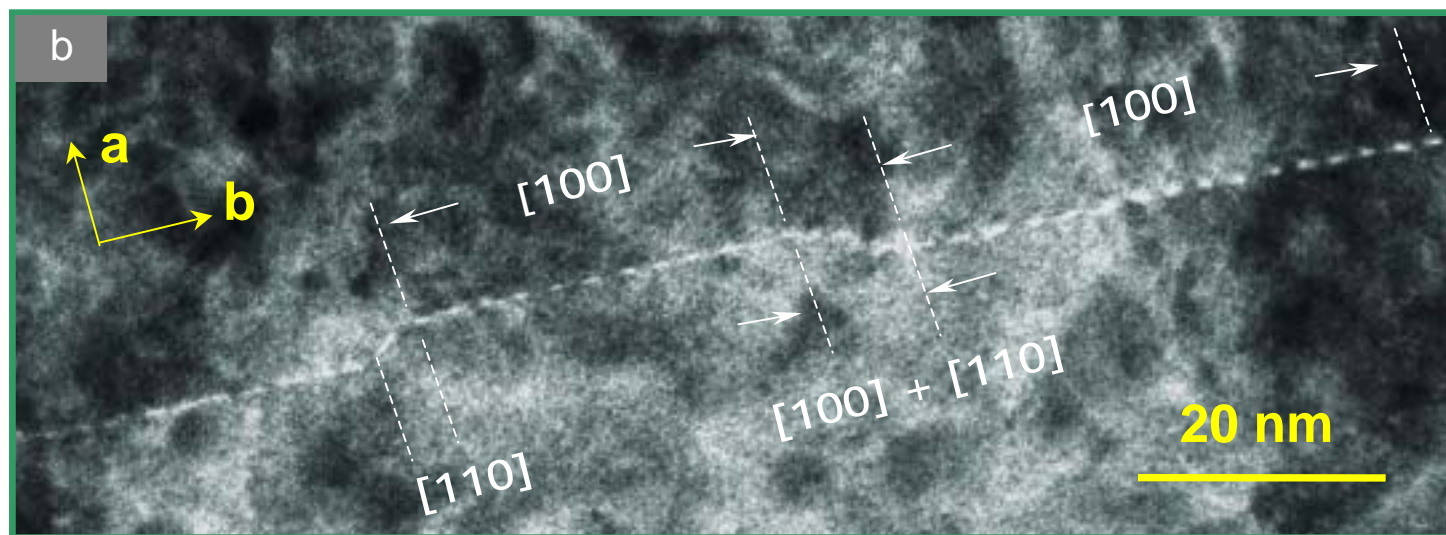
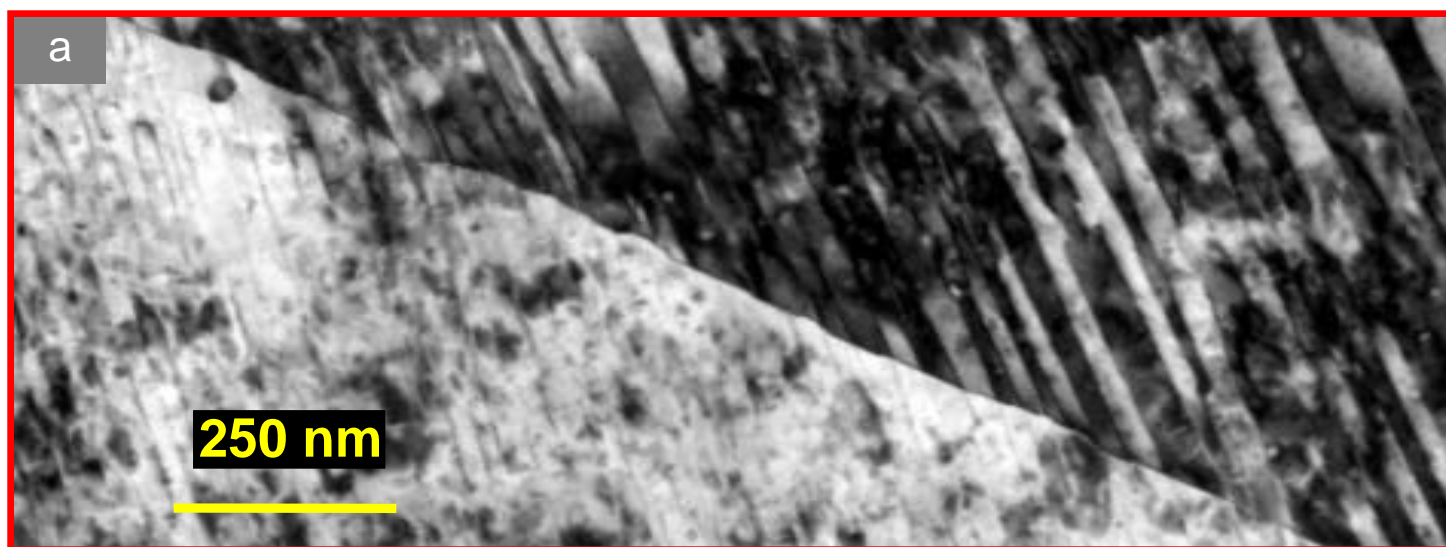


Figure 2

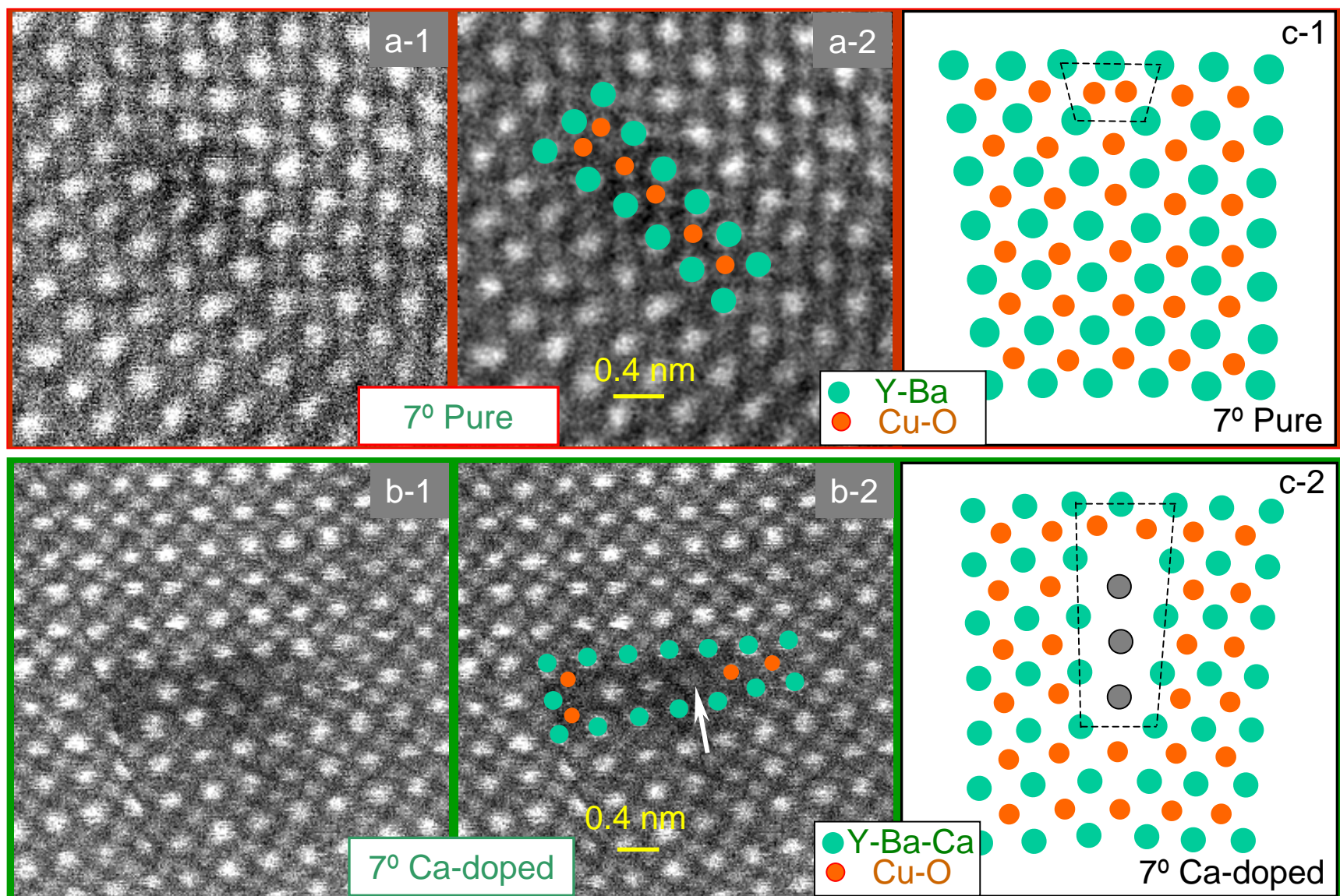


Figure 3

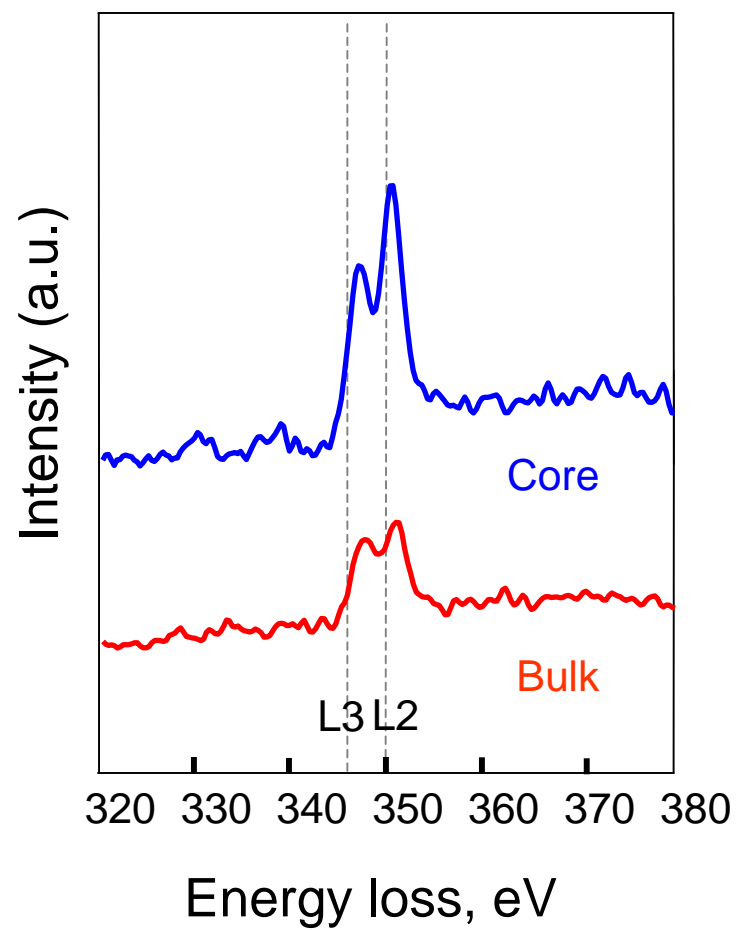


Figure 4 (a)

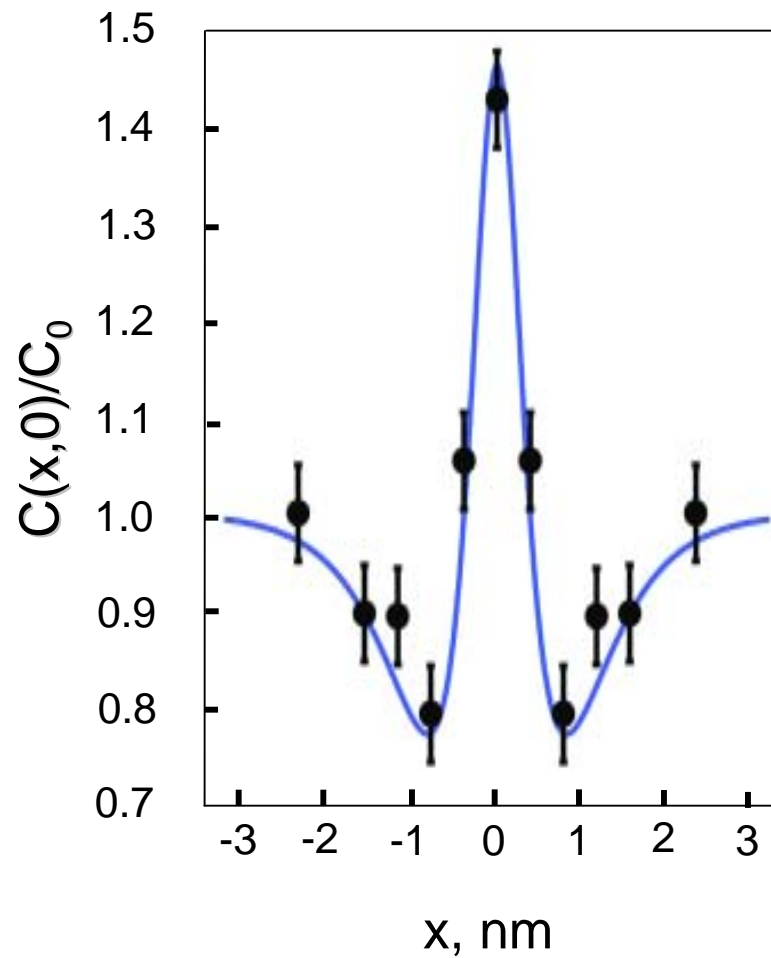


Figure 4 (b)

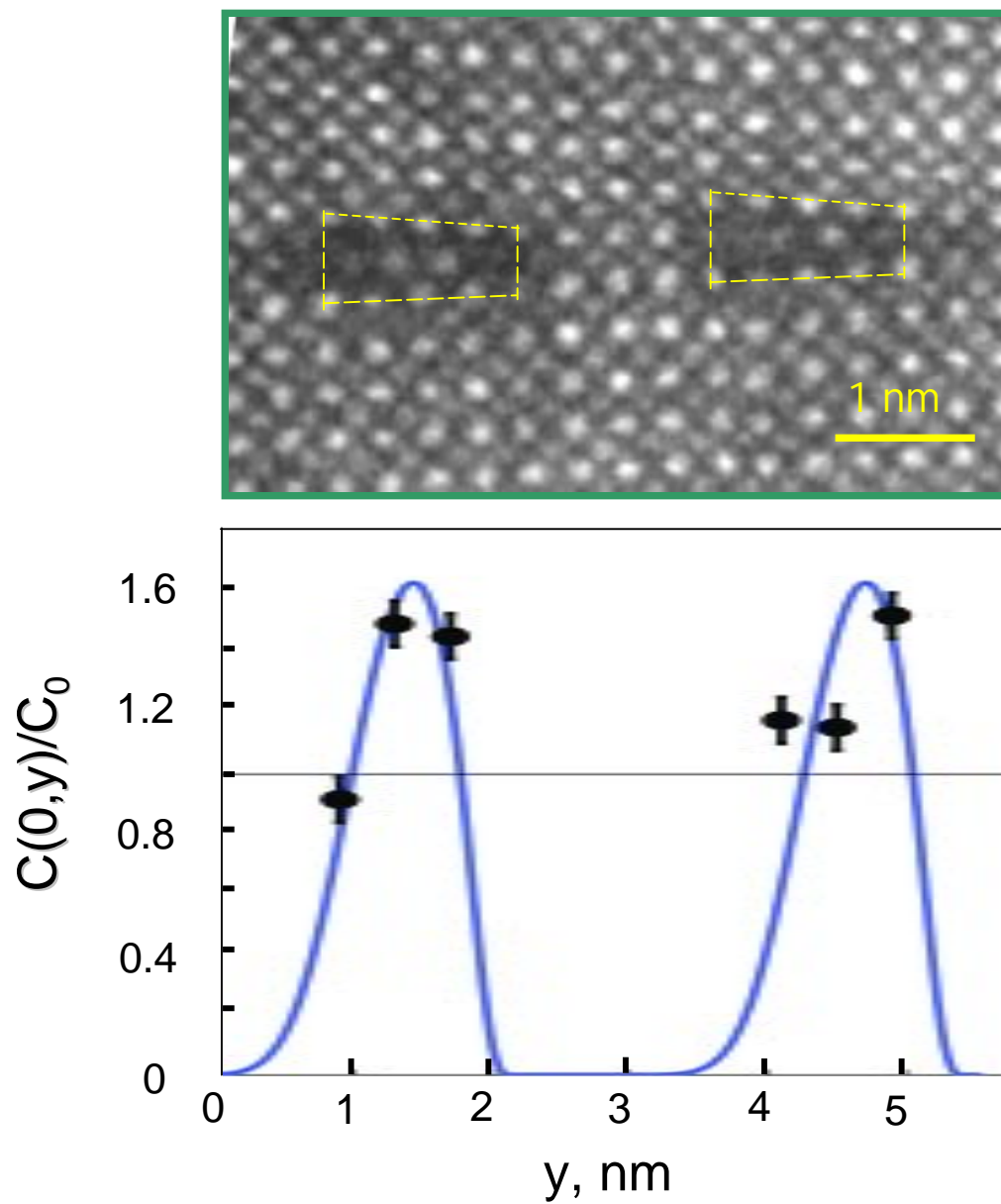


Figure 4 (c)

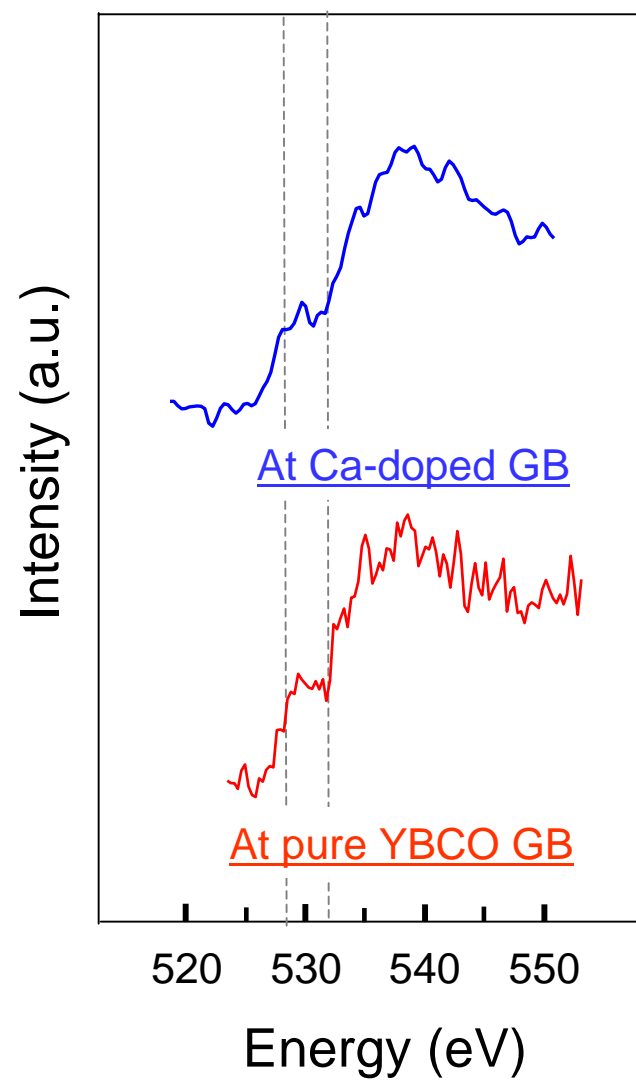


Figure 5

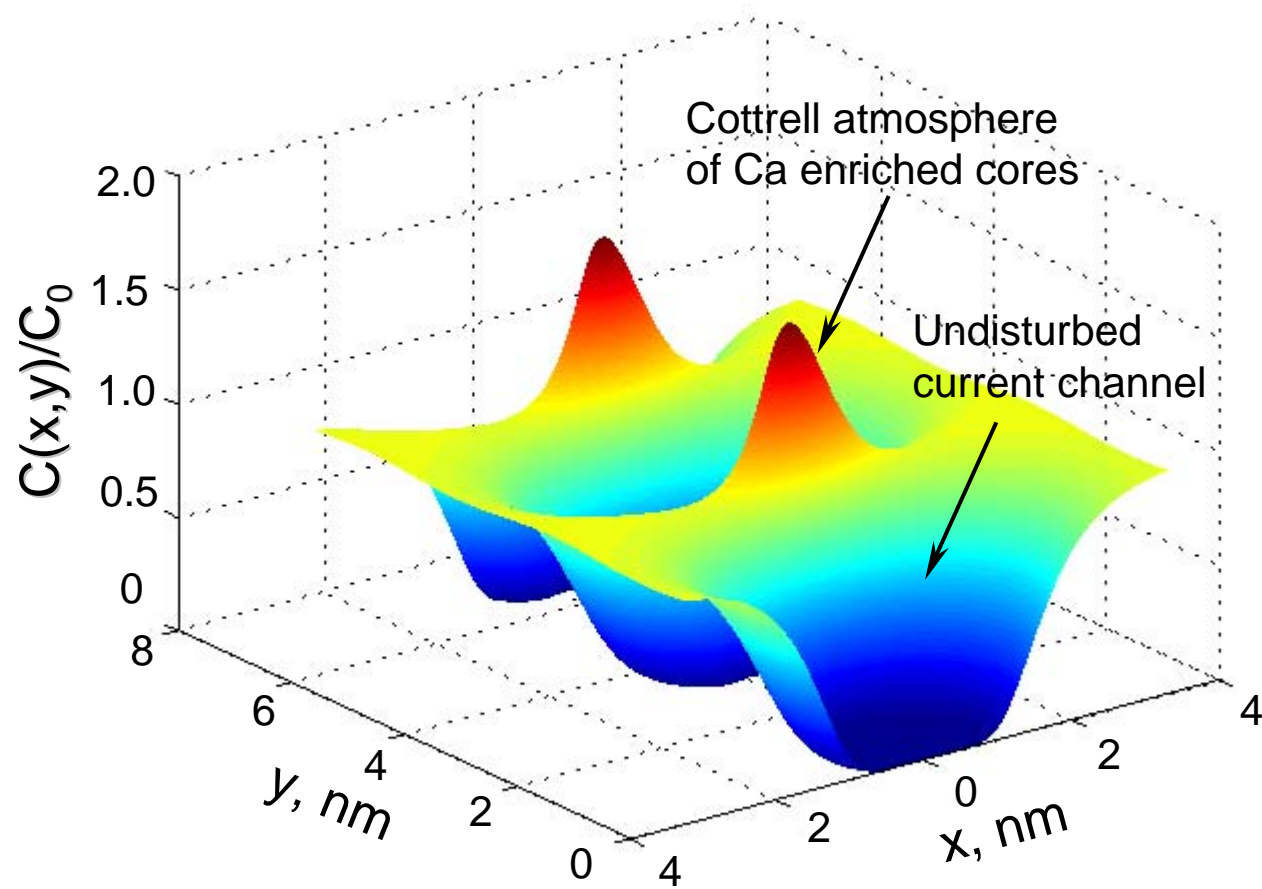


Figure 6